



A Simultaneous Dual-site Technosignature Search Using International LOFAR Stations

Downloaded from: <https://research.chalmers.se>, 2024-05-04 22:39 UTC

Citation for the original published paper (version of record):

Johnson, O., Gajjar, V., Keane, E. et al (2023). A Simultaneous Dual-site Technosignature Search Using International LOFAR Stations. *Astronomical Journal*, 166(5).
<http://dx.doi.org/10.3847/1538-3881/acf9f5>

N.B. When citing this work, cite the original published paper.



A Simultaneous Dual-site Technosignature Search Using International LOFAR Stations

Owen A. Johnson^{1,2,3}, Vishal Gajjar^{2,4}, Evan F. Keane^{1,5}, David J. McKenna^{1,6}, Charles Giese^{1,7}, Ben McKeon^{5,8}, Tobia D. Carozzi⁹, Cloe Alcaria^{1,10}, Aoife Brennan^{1,5,11}, Bryan Brzycki², Steve Croft^{2,4}, Jamie Drew¹², Richard Elkins², Peter T. Gallagher⁶, Ruth Kelly¹³, Matt Lebofsky², Dave H. E. MacMahon², Joseph McCauley¹, Imke de Pater², Shauna Rose Raeside^{1,6,14}, Andrew P. V. Siemion^{2,4}, and S. Pete Worden¹²

¹ School of Physics, Trinity College Dublin, College Green, Dublin 2, Ireland; ojohnson@tcd.ie

² Breakthrough Listen, University of California, Berkeley, 501 Campbell Hall 3411, Berkeley, CA 94720, USA

³ School of Physics, O'Brien Centre for Science North, University College Dublin, Belfield, Dublin 4, Ireland

⁴ SETI Institute, 339 Bernardo Avenue Suite 200 Mountain View, CA 94043, USA

⁵ School of Natural Sciences, Ollscoil na Gaillimhe—University of Galway, University Road, H91 TK33, Galway, Ireland

⁶ School of Cosmic Physics, Dublin Institute for Advanced Studies, 31 Fitzwilliam Place, Dublin 2, Ireland

⁷ Max-Planck-Institut für Radioastronomie, Bonn, Germany

⁸ Department of Physics, University of Limerick, V94 T9PX, Limerick, Ireland

⁹ Department of Space, Earth and Environment, Chalmers University of Technology, Onsala Space Observatory, SE-439 92 Onsala, Sweden

¹⁰ Département de Physique, Université Paul Sabatier, Toulouse, France

¹¹ European Southern Observatory, Alonso de Córdova 3107, Vitacura, Región Metropolitana, Chile

¹² The Breakthrough Initiatives, NASA Research Park, Boulevard 18, Moffett Field, CA 94035, USA

¹³ Mullard Space Science Laboratory, Department of Space and Climate Physics, UCL, Surrey RH5 6NT, UK

¹⁴ School of Physical Sciences and Centre for Astrophysics & Relativity, Dublin City University, Glasnevin, D09 W6Y4, Ireland

Received 2023 July 31; revised 2023 August 29; accepted 2023 September 1; published 2023 October 24

Abstract

The Search for Extraterrestrial Intelligence aims to find evidence of technosignatures, which can point toward the possible existence of technologically advanced extraterrestrial life. Radio signals similar to those engineered on Earth may be transmitted by other civilizations, motivating technosignature searches across the entire radio spectrum. In this endeavor, the low-frequency radio band has remained largely unexplored; with prior radio searches primarily above 1 GHz. In this survey at 110–190 MHz, observations of 1,631,198 targets from TESS and Gaia are reported. Observations took place simultaneously with two international stations (noninterferometric) of the Low Frequency Array in Ireland and Sweden. We can reject the presence of any Doppler drifting narrowband transmissions in the barycentric frame of reference, with equivalent isotropic radiated power of 10^{17} W, for 0.4 million (or 1.3 million) stellar systems at 110 (or 190) MHz. This work demonstrates the effectiveness of using multisite simultaneous observations for rejecting anthropogenic signals in the search for technosignatures.

Unified Astronomy Thesaurus concepts: [Astrobiology \(74\)](#); [Search for extraterrestrial intelligence \(2127\)](#); [Exoplanets \(498\)](#); [Technosignatures \(2128\)](#); [Radio astronomy \(1338\)](#)

Supporting material: machine-readable tables

1. Introduction

In the last 50 yr, evidence has steadily mounted that the constituents and conditions necessary for life are common in the Universe (Wordsworth & Pierrehumbert 2014). Predicting specific properties of electromagnetic emissions from extraterrestrial technologies is one of the most challenging aspects of searching for life in the Universe. However, it also represents a high-risk, high-reward endeavor. If an extraterrestrial civilization were intentionally attempting to indicate its presence through such emissions, it would be advantageous to make the signals easily distinguishable from natural phenomena. The evidence of such emissions is referred to as “technosignatures,” and the field dedicated to their detection is known as the Search for Extraterrestrial Intelligence (SETI).

It is commonly assumed that civilizations elsewhere in the Universe may employ similar technologies to those developed on Earth. Consequently, radio frequencies are considered a logical domain for conducting SETI surveys, due to the

widespread use of telecommunications and radar. Therefore, radio astronomy has played a significant role in the field of SETI since the 1960s (Drake 1961; Tarter et al. 1980). Numerous previous SETI surveys have utilized large single-dish telescopes operating at frequencies $\gtrsim 1$ GHz (Tarter 1996; Siemion et al. 2013; Enriquez et al. 2017).¹⁵ However, exploration of the radio window below 1 GHz has been relatively limited. Technosignature searches commonly seek narrowband (approximately Hz-scale) radio emissions, either transmitted directly or leaking from other civilizations. Nonetheless, there is no inherent preference for any specific segment of the radio spectrum, which necessitates surveys spanning from low frequencies (30 MHz) to high frequencies (100 GHz; Ng et al. 2022). At 30 MHz, it becomes very difficult to observe from the ground, due to ionospheric conditions (see Burke et al. 2019, chap. 7.8). This study primarily focuses on low-frequency SETI in the 110–190 MHz range.

1.1. Scientific Motivation

Low-frequency radio SETI presents significant challenges due to higher sky temperatures, which limit the sensitivity of



Original content from this work may be used under the terms of the [Creative Commons Attribution 4.0 licence](#). Any further distribution of this work must maintain attribution to the author(s) and the title of the work, journal citation and DOI.

¹⁵ See Wright (2018) for a review.

the underlying observations. The Murchison Widefield Array (MWA; Tingay et al. 2013) in Western Australia has been at the forefront of low-frequency SETI research thus far (Tingay et al. 2016, 2018a, 2018b). However, the LOw Frequency ARray (LOFAR) presents a compelling scientific case for conducting a SETI survey (Loeb & Zaldarriaga 2007). Aside from operating at low frequencies in the northern sky, LOFAR offers a large field of view, enabling the search for technosignatures across thousands of stars in each observation.

Radio SETI also grapples with the challenge of handling a significant amount of radio frequency interference (RFI). Traditionally, SETI surveys have been conducted using single-dish radio telescopes. While these telescopes offer operational convenience and room for upgrades, they possess limitations in effectively distinguishing between sources of interference and authentic sky-bound signals unless equipped with multibeam receivers. In contrast, the utilization of two local LOFAR stations presents two notable advantages over conventional single-dish surveys. As demonstrated in studies conducted by Enriquez et al. (2017) and Price et al. (2020), single-dish surveys typically employ an “ON” and “OFF” observing technique, where the target is observed for five minutes (“ON”) followed by five minutes of observing a different location (“OFF”). This cycle is repeated three times, resulting in three “ON” pointings and three “OFF” pointings. This approach facilitates the identification and elimination of narrowband signals detected in the local environment that could potentially interfere with the search for technosignature candidates. By employing multiple stations, the search benefits from the unique local RFI environments at each station. This leads to a higher rate of rejecting false-positive signals compared to the aforementioned surveys, which have signals of interest on the order of thousands. Additionally, because there are two stations involved, there is no requirement to alternate between an “ON” and “OFF” observation regime. As a result, the entire observation duration can be dedicated to directly observing the target, as the comparison of RFI environments would yield the same effect. This characteristic renders SETI surveys with two or more telescopes a highly valuable resource, in particular in today’s RFI environments.

1.2. Breakthrough Listen

The Breakthrough Listen (BL) program is conducting one of the most comprehensive searches for evidence of intelligent life by extending the search to a wide variety of targets from existing ground-based observing facilities (see Gajjar et al. 2019 for a review). All of the existing observations within the BL program have so far been conducted in the 1–27.45 GHz range (Ng et al. 2022). In this paper, we report on low-frequency extension of the BL initiative using two international LOFAR stations to perform simultaneous dual-site observations of nearby exoplanet candidates of interest from both the Transiting Exoplanet Survey Satellite (TESS; Ricker et al. 2015) and from Gaia (Gaia Collaboration et al. 2018) in collaboration with the BL program. This survey also demonstrates the proof of concept of using dual-site observations for the rejection of spurious local sources of terrestrial origin. This method thus removes the need for separate “ON” and “OFF” pointings (Gajjar et al. 2021). In Section 2, we describe the observational set up and the data acquired. Section 3 explains the data analysis steps taken. We discuss the

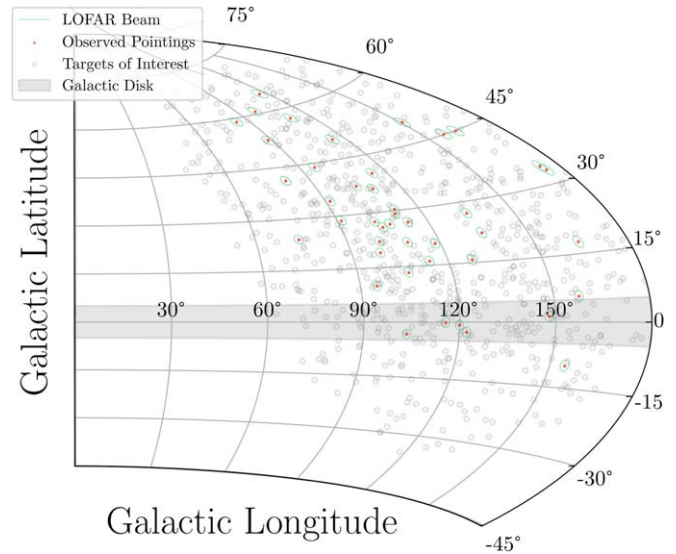


Figure 1. An Aitoff projection of the sky in Galactic coordinates depicts the distribution of survey pointings, with the Galactic disk shaded in gray. Gaia sources are omitted from the plot due to their extremely high source density. Gray dots represent TESS Targets of Interest (ToIs). Those targets observed during our survey are marked with red dots at boresight, with green showing the half-power beamwidth ($2^{\circ}59'$).

implications of this work in Section 4 before concluding in Section 5.

2. Observations

This study encompasses a total of 44 targeted pointings, where each pointing consists of a 15 minute scan centered on specific targets selected from the TESS catalog, focusing on confirmed or candidate exoplanets (refer to Figure 1). The entire observation campaign spanned a duration of 11 hr, covering an area of 232 deg^2 in the northern sky.

2.1. LOFAR

LOFAR, a pioneering low-frequency aperture array telescope, spans hundreds of kilometers across Europe and serves as a pathfinder to the Square Kilometer Array (SKA). The array consists of a core station with outrigger stations situated in the Netherlands and additional international stations spanning multiple countries, such as Germany, France, Sweden, Ireland, Latvia, Poland, and the United Kingdom. Additionally, stations are currently in the process of being constructed in Italy and Bulgaria. The LOFAR array operates using two types of antenna, the Low Band Antenna (LBA) and the High Band Antenna (HBA), operating at 10–90 MHz and 100–250 MHz respectively. In this study, the HBAs at the Irish and Swedish LOFAR station are used to carry out observations noninterferometrically. The field of view (FoV) of an international LOFAR station is rather large; at full width at half maximum, it is 5.3 , 3.4 , and 2.3 deg^2 at frequencies of 120, 150, and 180 MHz, respectively (van Haarlem et al. 2013). With such a large region where our observations are sensitive, each pointing contains millions of stars that can be searched for technosignatures (Włodarczyk-Sroka et al. 2020). In this survey, in addition to the 44 TESS targets at boresight, 1,631,152 Gaia targets are covered by our observations and so are searched for technosignatures.

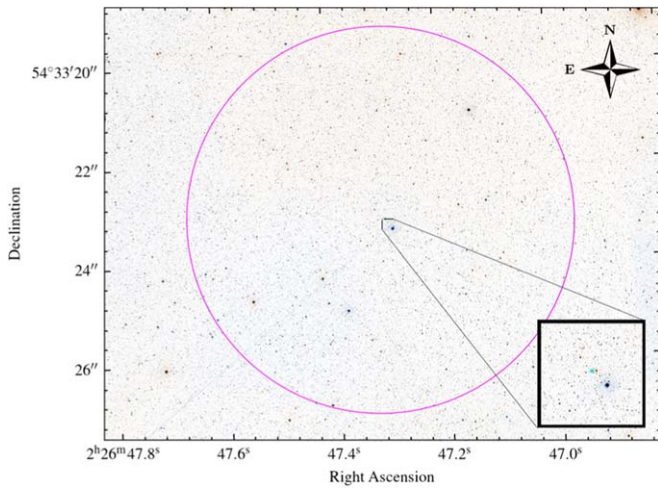


Figure 2. This figure illustrates one of the boresight pointings directed at a TESS object (highlighted in green), with the LOFAR beam’s full width at half maximum (FWHM) shown in pink. The background image is from the Sloan Digital Sky Survey (SDSS; Albareti et al. 2017).

2.2. Targets

A significant fraction of radio emission from Earth is emitted in the direction of the ecliptic plane. For example, powerful planetary radars are used to explore Solar System objects (Siemion et al. 2013), and high-powered transmitters are used to communicate with Solar System probes (Enriquez et al. 2017). It is conceivable then that such leakage radiation may also be emanating from other worlds, preferentially in their planetary orbital planes. This is why we chose TESS targets, as these are the closest transiting exoplanet systems known (Borucki et al. 2008; Ricker et al. 2015). Observing these sources with the LOFAR HBAs enables robust constraints on any associated artificial low-frequency radio emission.

2.2.1. TESS Targets

In order to determine a target list for this work, the latest list of TESS object of interests (TOIs) was retrieved (NASA Exoplanet Science Institute 2022) and a shortlist of targets were obtained rejecting possible false positives. Because the sensitivity of the HBA array is best $\pm 30^\circ$ of zenith, the required overlap for both LOFAR international stations spans the decl. range $+27^\circ$ to $+83^\circ$. Further practical considerations were also accounted for, i.e., to stay as far from bright sources like the Sun as possible at both sites, and to balance sensitivity at both sites (Johnson 2023).¹⁶ We report observations toward 44 unique targets from the TESS catalog in this study, where each target was observed for 15 minutes. Figure 1 shows the distribution of these targets observed in comparison to the pool of all TESS TOIs.

2.2.2. Gaia Sources

The beam of a LOFAR station has an expansive coverage enabling observation of a substantial number of stars in the field of view. The significance of these in-field stars has been highlighted by Włodarczyk-Sroka et al. (2020). Consequently, during our observations targeting 44 sources from the TESS catalog, we encountered a significant number of in-field stars within our field of view, as shown in Figure 2.

To determine the list of targets within this field of view, we utilized the Gaia catalog. Some previous major SETI surveys focused their searches toward Sun-like stars (Tarter 1996). However, because our understanding of the origin of life is limited, it makes sense to allow for the possibility of life arising on a planet that is neither Earth-like nor around stars that are Sun-like. Similarly, we should consider planets not necessarily located in the habitable zone. This is typically characterized as the orbital range wherein liquid water could exist (Kasting et al. 1993), as inferred from planetary equilibrium temperatures often ignoring the unknown albedo of the exoplanets. Any sensitive radio SETI survey seeking to maximize the chance of detecting weak radio signals should, insofar as possible, expand its search to encompass nearby stars of a broad range of spectral types and with exoplanets of all sizes and distances from their parent star. Thus, we conducted calculations to determine the number of Gaia stars with a mean distance of 1215 pc, with an accuracy in their distances of at least 20%.

This study used Gaia’s third data release (GDR3; Ginsburg et al. 2019; Gaia Collaboration et al. 2023). When analyzing GDR3, two filters were applied to the survey volume and sensitivity accuracy of the in-beam target values. First, a constraint on the R.A. and decl. errors was implemented. If a Gaia source was found to be in the beam but had an error magnitude greater than the FWHM, it was removed from the source pool. Equation (1) states the first condition of filtering:

$$\theta_{\text{sep}} + \sqrt{\Delta \text{R.A.}^2 + \Delta \text{decl.}^2} < 1^\circ.295. \quad (1)$$

As the sensitivity of the survey is calculated based on a source’s distance, a second filter is implemented to remove sources that have large errors. By taking the difference ($\Delta \sigma_G$) in the upper and lower confidence levels of GSP-Photometry,¹⁷ we obtain a percentage error on distance. All sources with a d_{M_G} error of 20% or greater are filtered out of the source list. Equation (2) states the second condition of filtering:

$$\frac{\Delta \sigma_G}{d_{M_G}} < 20\%. \quad (2)$$

A total of 1,631,152 stars form this list, making it one of the largest samples of stars ever surveyed for SETI purposes. Figure 3 shows a Hertzsprung–Russell diagram for the targets.

2.3. Simultaneous Observations

Typically, international LOFAR stations operate as stand-alone telescopes 2–3 days per week, i.e., they do not operate as part of the International LOFAR Telescope’s Europe-wide array. This project was undertaken during this stand-alone time. For this purpose, the international LOFAR in Stand-Alone mode (iLiSA) package¹⁸ is used to control both telescopes simultaneously. iLiSA provides a high-level operational control of multiple LOFAR stations, including scheduling, processing pipeline dispatching, and metadata aggregation (see Figure 5). For the observations in this study, an operator-produced list of targets that were close¹⁹ to the local meridian

¹⁷ SQL Keys: distance_gspphot, distance_gspphot_upper (d_{M_G}) and distance_gspphot_lower.

¹⁸ <https://github.com/2baOrNot2ba/iLiSA/releases/tag/v6.1>

¹⁹ In practice, as Birr and Onsala are separated by $\sim 20^\circ$ of longitude, the optimum scheduling is to observe ~ 40 minutes $-T_{\text{obs}}/2$ “late” at Onsala and 40 minutes $+T_{\text{obs}}/2$ “early” at Birr.

¹⁶ These selection criteria were applied using a custom-developed dual-site observation planning software.

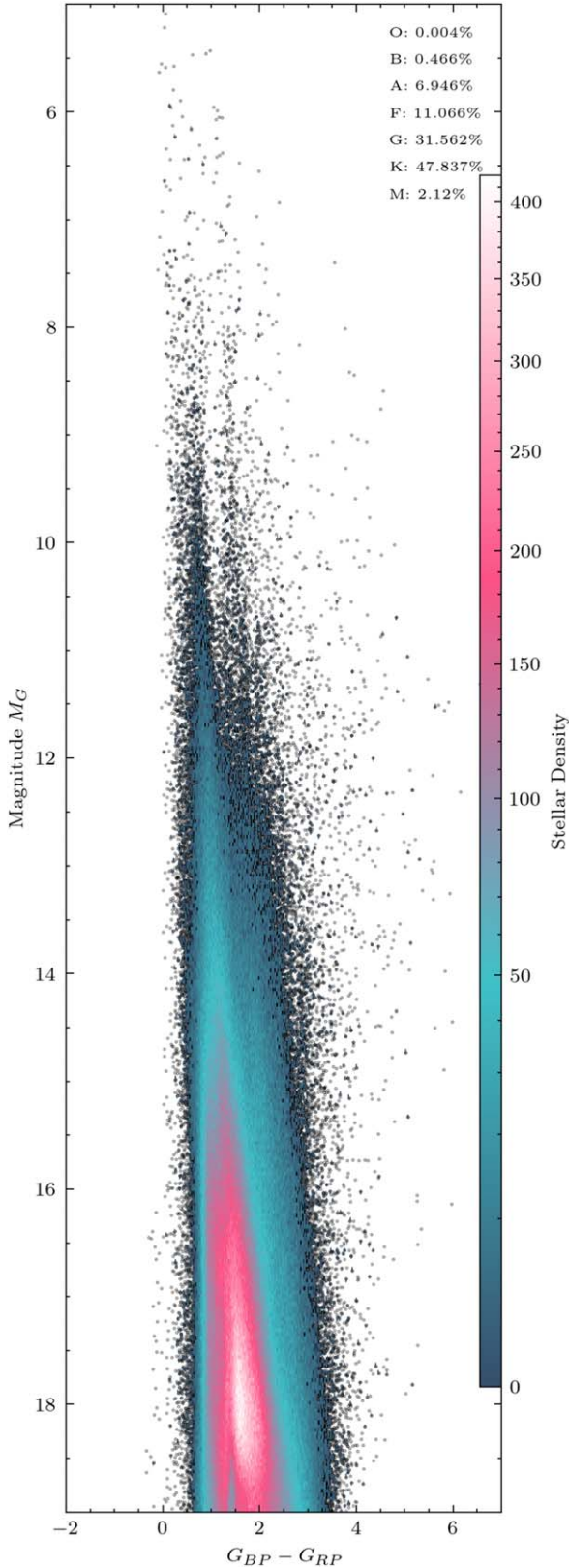


Figure 3. A Hertzsprung–Russell diagram of the 1,631,198 Gaia targets searched for technosignatures in this survey, with a mean distance of 1270 pc. The relative distribution with respect to spectral type is O < 0.01%, B—0.4%, A—6.94%, F—11.01%, G—31.56%, K—47.84%, M—2.12%. This is as opposed to the distribution of the general Gaia catalog, which is O, B < 0.0001%, A—1.5%, F—18.9%, G—44.4%, K—34.5%, M—0.6%.

Table 1

Specifications for the Data Input to Our Processing Pipeline after Pre-processing and Preparing the Raw Data with `udpPacketManager` (McKenna et al. 2023a)

Data Attribute	Value
Frequency Start (f_{start})	109.9609375 MHz
Frequency End (f_{end})	190.0390625 MHz
Frequency Resolution	2.980232239 Hz
Channel Number	27000832
Obs. Length (t_{obs})	15 minutes
Temporal Resolution	0.67108864 s
Maximum Drift-rate Search	$\pm 4 \text{ Hz s}^{-1}$
S/ N_{min} threshold	10

was fed into `iLiSA` at each epoch. Toward each target, one beam per station was formed using `iLiSA`, and each beam was formed with 412 HBA subbands (corresponding to a bandwidth of 80.46875 MHz). The scan time on each target was 15 minutes, and the whole scheduling block was a few hours per epoch.

In this study, the only `iLiSA` pipeline used was the raw data recorder, which simply receives UDP packets of beam-formed data and writes them to disk, separately at each site. The data consist of coarse-channelized complex voltages. The initial data stream is two polarizations from each antenna. With real Nyquist sampling with a 200 MHz clock and coarse-channelization factor of 512 taking place, only 488 (244) of these are recordable when the data are written as 8-bit (16-bit) complex numbers. Further processing of these data is necessary, and we use `udpPacketManager` (McKenna et al. 2023a) to ultimately create total intensity `sigproc` (Lorimer 2011) formatted filterbank files at the time and frequency resolution appropriate for our Doppler-drift search, shown in Table 1.

3. Analysis

The most common transmissions sought in SETI searches are narrowband ($\sim \text{Hz}$) radio signals. Ubiquitous in early terrestrial communication systems, such signals can be produced with relatively low energy and traverse the interstellar medium easily. They also can be readily distinguished from natural astrophysical sources. These signals could either be transmitted intentionally or arise as leakage from extrasolar technologies. The apparent frequency of a distant narrowband transmitter is expected to exhibit Doppler drift due to the relative motion between the transmitter and receiver. The Breakthrough Listen group has developed an efficient narrowband search software package that includes a search for such drifting signals, named `turboSETI` (Enriquez et al. 2017), which we use for the analysis of our LOFAR survey data. However, before we can compare narrowband signal hits detected using this tool, it is necessary to compare them in the barycentric reference frame.

3.1. Barycentric Correction

The movement of the Earth around its axis and the Sun introduces a Doppler effect that causes radio signals' frequency

Table 2

Comparison of the Number of Narrowband Signals Detected for a Subset of TESS Objects in Both the Topocentric and Barycentric Reference Frames

TIC ID	LOFAR-SE Hits	I-LOFAR Hits Topocentric Results	Mutual Hits	LOFAR-SE Hits	I-LOFAR Hits Barycentrically Corrected Results	Mutual Hits
121966220	387	178	18	376	171	0
249862365	340	193	22	330	196	0
250724252	276	190	21	265	262	0
27677846	313	159	20	294	151	0
470315428	384	175	17	356	224	0

Notes. `turboSETI` searches were completed using identical parameters in each reference frame. We did find a small number of mutual hits, while it was found that barycentrically correcting the data prior to searching filtered out all prior mutual hits of interest.

Table 3

TESS Candidates Used as Boresight Pointings for Survey

TIC ID	MBJD Start	R.A. J2000 hr	Decl. J2000 Deg	Distance (pc)	LOFAR-SE Hits	I-LOFAR Hits	Mutual Hits
27677846	59410.3856	4.424676	46.365902	78.71 ± 0.330	294	151	0
51024887	59410.3189	2.810346	62.189260	41.53 ± 0.158	265	181	0
81831095	59410.3300	3.187109	61.762385	399.40 ± 5.300	277	196	0
121966220	59410.3967	5.053188	41.785784	472.70 ± 9.135	376	171	0
142090065	59402.4266	5.271567	79.737727	182.91 ± 1.291	290	282	0
191146556	59410.4078	0.553625	46.340305	282.83 ± 3.011	378	266	0
249862365	59410.3078	2.541534	52.704091	184.69 ± 1.290	330	197	0
250724252	59410.2967	2.233683	53.121508	$574.87 \pm \dots$	265	262	0
266500992	59410.3634	4.078149	52.256992	165.31 ± 0.987	276	164	0
288132261	59403.5613	13.965621	79.583322	154.94 ± 0.521	328	310	0

First 10 entries of the table. Full table available in a machine-readable format in the online journal.

Notes. These targets were obtained from the NASA Exoplanet Archive (NEA) Targets of Interest database. Selection criteria were based on what targets were visible at both stations. The above table contains parameters relevant to each observed target and the resultant hits attained from the narrowband search at respective stations. A* denotes a confirmed exoplanet in the NEA. The distance is inferred from Bailer-Jones et al. (2018), which makes use of GDR2 parallax values.

(This table is available in its entirety in machine-readable form.)

and arrival time to shift as

$$f_{\text{obs}} = f_{\text{em}}(1 - v_{\text{rel}}). \quad (3)$$

Here, f_{obs} is the observed frequency, f_{em} is the emitted frequency (or barycentric frequency), and v_{rel} is the velocity of the source relative to the observer, normalized by the speed of light. The Doppler effect only depends on the velocity of the source relative to the observer, and for a source moving toward the observer, we can consider $-v_{\text{rel}}$, while for a source moving away from the observer, we consider $+v_{\text{rel}}$. The relative velocity between the observer and the source will differ for different observing epochs, the location of the source in the sky, and the geographical location of the telescope. For instance, the target TIC 27677846 was observed on UT 2021 July 15, from both the LOFAR stations simultaneously. The expected relative velocity (v_{rel}) toward the source was -7.669×10^{-5} and -7.496×10^{-5} , causing a relative shift ($f_{\text{em}} - f_{\text{obs}}$) of $+11.504$ kHz and $+11.246$ kHz for a hypothetical ETI signal transmitted at a constant frequency of 150 MHz observed at the Sweden and Ireland stations, respectively. These are significant shifts that are distinct at the two stations, and they need to be corrected to compare the same signal observed at the two stations.

Typically, barycentric corrections are introduced by adjusting the local oscillator during observations. However, in our study, we record beam-formed baseband voltages during

observations and produce three different data products with varying temporal and spectral resolutions during post-processing (Lebofsky et al. 2019). We are interested in searching for a wide variety of signals, including narrowband signals, broadband transient signals, and wideband pulsating signals. Introducing local oscillator shifts during observations can impact our other signal searches. Therefore, we correct for barycentric drift after the channelization and detection of the baseband voltages for narrowband signal searches using software that we have developed.²⁰ Details of this correction and code (Gajjar 2023) are fully discussed in Appendix A. For comparison, both topocentric and barycentric data are analyzed for a small subset of the targets, and the results are shown in Table 2.

3.2. Searching for Narrowband Signals

Using `turboSETI` with the parameters outlined in Table 1, a Doppler-drift search was carried out on the observed candidates listed in Tables 3 and 4 at both stations. This resulted in the list of “hits” collected in Tables 3 and 4, where hits are defined as a narrowband signal detected above the given threshold, $S/N = 10$. The distribution of narrowband signals detected at both stations is shown in Figure 6. A large percentage of hits are seen at both sites in the 120–140 MHz

²⁰ <https://github.com/gajjar/BaryCentricCorrection>

Table 4
Gaia Candidates Found within 1°295 of TESS Boresight Pointing

Gaia DR3 ID	R.A. J2000 Deg	Decl. J2000 Deg	Distance (pc)	T_{eff} (K)	Pointing Separation (deg)	TIC ID	I-LOFAR Hits	LOFAR-SE Hits	Mutual Hits
564235797910436864	8.86126	77.85329	781.699	4014.7295	0.009	407394748	181	257	0
564235802207784960	8.87885	77.85548	1253.498	5646.9490	0.010	407394748	181	257	0
564235763550696832	8.84236	77.84989	1156.965	4437.7656	0.011	407394748	181	257	0
564235797910441344	8.90038	77.85941	1578.279	4833.3310	0.013	407394748	181	257	0
564236111445430784	8.94834	77.85299	1757.851	5909.2330	0.014	407394748	181	257	0
564235802207784320	8.89499	77.86029	1015.023	4973.0776	0.014	407394748	181	257	0
564235729190956544	8.96611	77.84246	1481.637	4466.9937	0.016	407394748	181	257	0
564238619706331520	8.80710	77.84626	1569.950	4931.5280	0.018	407394748	181	257	0
564238619706331392	8.79529	77.84677	1212.563	5220.9077	0.020	407394748	181	257	0
564236180164905344	8.90174	77.86865	2039.539	4982.6694	0.022	407394748	181	257	0

First 10 entries of the table. Full table available in a machine-readable format in the online journal.

Notes. GDR3 targets that exhibit a distance error of 20% or more are cut from the data set as constraint calculations are distance dependent. The above table contains the details of each Gaia target found in a specific TESS pointing and associated separation from the boresight of the LOFAR beam.

(This table is available in its entirety in machine-readable form.)

range. This falls within the range of expected RFI leakage seen from neighboring airports.²¹

Using a drift-rate search of $\pm 4 \text{ Hz s}^{-1}$ for this study covers a fraction of the possible drift rates of transmitters from exotic objects that can be detected as outlined by Sheikh et al. (2019). Li et al. (2022) show that 4 Hz s^{-1} is comprehensive in relation to the expected distribution of exoplanet drift rates. The omission of a search in this parameter space is due to its computationally intense nature of searching for narrowband signals across a sizeable drift-rate range. However, in doing this, the parameter space searched for ETI signal has been drastically reduced. Continual development of search algorithms like *turboSETI* is progressing to make larger drift-rate searches more computationally feasible.

Upon first inspection of Figure 6, it appears that the results at both stations are somewhat similar. However, upon performing a Kolmogorov–Smirnov (KS) test for each set of results for drift rate, S/N, and frequency of detected hits, the highest p -value returned was on the order of 10^{-11} , indicating that the RFI environments at each of the stations are significantly different.

3.3. Dual-site Coincidence Rejection

In the case of this study, a singular beam observes a single and background target (see Figures 2 and 4) target for 15 minutes at both stations, and observations are converted to barycentric reference frame. Narrowband searches are then performed at both sites, and the results of both searches are compared. Figure 8 shows two common detection cases and how the use of dual-site observation aids in discerning the nature of each signal’s origin.

Case A: In this case, a hit has been detected at the Irish station but is absent from the same frequency at the Swedish station. Thus, the signal is rejected as a extraterrestrial emitter and deemed as RFI local to the Irish station.

Case B: Similar to case A, but this time the converse is seen, a hit has been detected at the Swedish station and not at the same frequency at the Irish station.

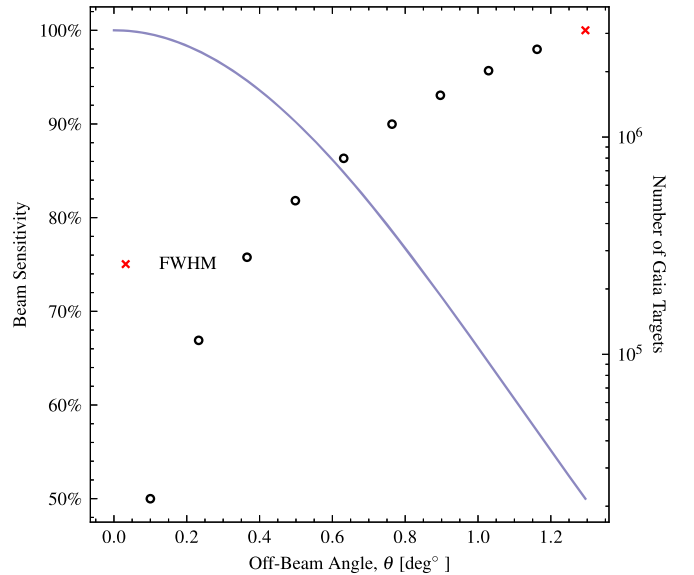


Figure 4. The LOFAR HBA beam’s sensitivity at 150 MHz changes in relation to the off-axis boresight angle (θ). Furthermore, a plot of the number of filtered Gaia targets within the beam pointing as a function of θ is presented. The \times represents the value for the FWHM of the beam.

In our analysis, a signal is classified as a mutual extraterrestrial hit only if two conditions are met: (a) the signals are within a frequency range of $\pm 4 \text{ Hz}$ of each other in the barycentric reference frame, and (b) their drift rates are within $\pm 0.2 \text{ Hz s}^{-1}$ of each other after barycentric drift corrections. In Figure 9, an intriguing candidate is depicted. In the topocentric frame, we detected a narrowband signal at 160 MHz that was simultaneously present at both stations. However, when converting to the barycentric reference frame (as illustrated in Figure 9), the signal appears to be seen at different frequencies with opposite signs, due to the different line-of-sight velocities toward the target. As a result, this narrowband signal is rejected as a genuine sky-bound signal.

3.4. Search Results

Figure 7 depicts the observed drift rates as a function of frequency. As shown in Figure 6, a substantial number of hits

²¹ Shannon & Goteborg Landvetter.

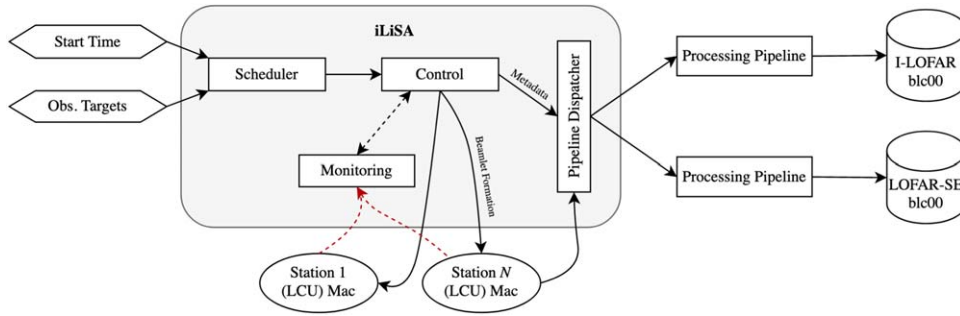


Figure 5. iLiSA block diagram, showing how an operator-defined schedule is ingested and is executed in a timely fashion. Data then begins to flow and ends up being ingested by processing pipelines together with associated metadata.

are observed at 125 and 138 MHz, suggesting the presence of potential aircraft communications within these frequency bands. Notably, at I-LOFAR, a significant number of hits are also detected at 167 MHz, which is suspected to be related to aircraft communication. Additionally, a pronounced spike in RFI at 164 MHz is observed at the Swedish station (LOFAR-SE), likely associated with marine communications due to the proximity of LOFAR-SE to the coast.

Implementing barycentric corrections and coincidence rejections, no signals of interest were identified among the observed candidates. Comprehensive information regarding the targets and their corresponding hits for both TESS and Gaia can be found in the supplementary databases presented in the Tables 3 and 4.

4. Discussion

4.1. Survey Sensitivity

The required power for a certain extraterrestrial intelligent (ETI) transmitter to be detected depends on its directionality and other signal characteristics. We can measure the transmitter power of an ETI beacon in terms of the effective isotropic radiated power (EIRP; Enriquez et al. 2017) as

$$\text{EIRP} = \sigma \times 4\pi d_\star^2 \frac{\text{SEFD}}{\delta\nu_t} \sqrt{\frac{\delta\nu}{n_p t_{\text{obs}}}} \text{ W}. \quad (4)$$

Here, σ is the required S/N, $\delta\nu$ is the bandwidth of the received signal, $\delta\nu_t$ is the transmitted bandwidth, t_{obs} is the observing integration time, SEFD is the System Equivalent Flux Density, n_p is the number of polarizations, and d_\star is the distance between the transmitter and the receiver, i.e., the distance to the star. We considered $\delta\nu_t$ to be 1 Hz. For the narrowband signals we consider in our Doppler searches, we assume $\delta\nu$ is matched to our spectral resolution and further assume a temporal duty cycle of 100%.

The SEFD of the international HBA stations used in this survey is on average ~ 900 Jy for most of the band, rising to ~ 1.2 kJy at the band edges (van Haarlem et al. 2013). For reference, the SEFD of the GBT at the 1.4 GHz is around 10 Jy. This difference in sensitivity is because sky temperature scales as $\nu^{-2.6}$, meaning it can be hundreds of times higher in the LOFAR band. However, the average values are of little use, as there is also a large degree of variation in the sky temperature across the sky. For this reason, we perform a separate calculation for every target to determine the relevant luminosity limit in each case. For example, the sensitivity to each off-boresight target is determined by its proximity to the pointing

coordinates. Figure 4 depicts both the impact on sensitivity and the number of background stars within a given LOFAR beam. Figure 2 shows an example pointing from the survey and also illustrates well the vast volume of targets that appear in a LOFAR beam (pink).

Figure 10 presents the luminosity limits for the cumulative targets of this survey within the frequency range of 110–190 MHz. In this figure, the limiting luminosity is compared to notable values of EIRP for various scenarios. These scenarios include a Kardashev I type advanced civilization transmitting at a power level of 10^{17} W, an advanced civilization producing planetary radar-level transmissions with a transmitting power of 10^{13} W, and a cumulative aircraft radar-type system transmitted across a large solid angle with a power of 10^{10} W (Siemion et al. 2013). The figure demonstrates that, due to the varying system temperature (T_{sys}) across the frequency band, our observations were sensitive to detecting a range of Kardashev I type targets. Specifically, we were able to detect approximately 25% of the targets at the lower end of the frequency band, increasing to nearly 80% of the targets at the higher end of the band.

4.2. Starlink Interference

A recent study by Di Vruno et al. (2023) has shown that unintended electromagnetic radiation (UEMR) from the Starlink satellite constellation produced broadband interference ranging from 0.1 to 10 Jy and narrowband interference ranging from 10 to 500 Jy. UEMR was detected at frequencies at 110–188 MHz, which is the bandwidth of the HBA used in this study. UEMR has many potential consequences for low-frequency radio observations. Analysis of turboSETI hit detection’s within 1 MHz the UEMR narrowband emission frequencies (125, 135, 143, 150, and 175 MHz; Di Vruno et al. 2023) show that 17.8% of total detected hits are within this region. This region occupies 18.5% of this study’s bandwidth. This result is expected, as although UEMR affects a number of different types of radio searches, it does not affect narrowband searches of this nature. This is due to two factors. First, satellites in Low Earth Orbit (LEO) to Geostationary orbit (GEO) usually have velocities that are too high for them to be detected with the temporal resolution of our data, and they are at drift-rate values outside the parameters of this search ($>4 \text{ Hz s}^{-1}$). Second, the satellites are in the near field of each station’s beam, and due to their relative distance to the observer compared to the boresight target, a satellite is less likely to appear in both beams simultaneously. It is concluded that the Starlink constellation does not add to the number of narrowband hits detected in this study.

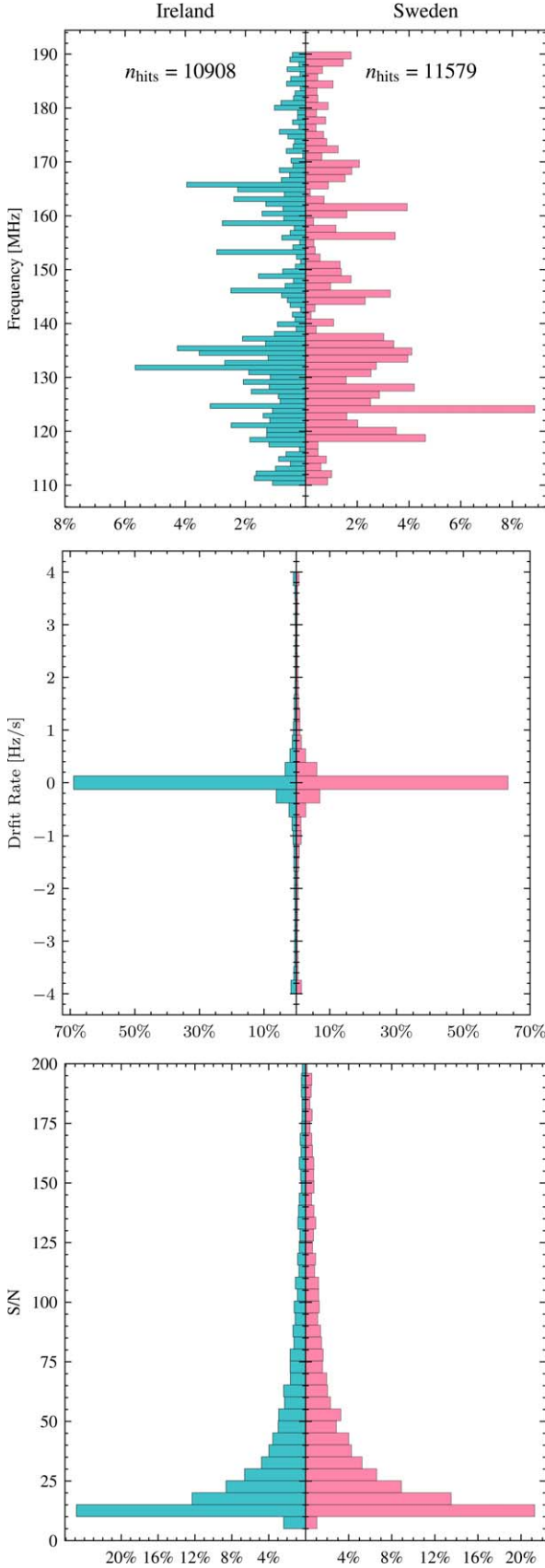


Figure 6. Comparison of drifting signals or “hits” detected at both stations seen across the HBA frequency band. Each bin within the data set represents a 1 MHz frequency range and is accompanied by a corresponding percentage indicating its proportion to the overall data set.

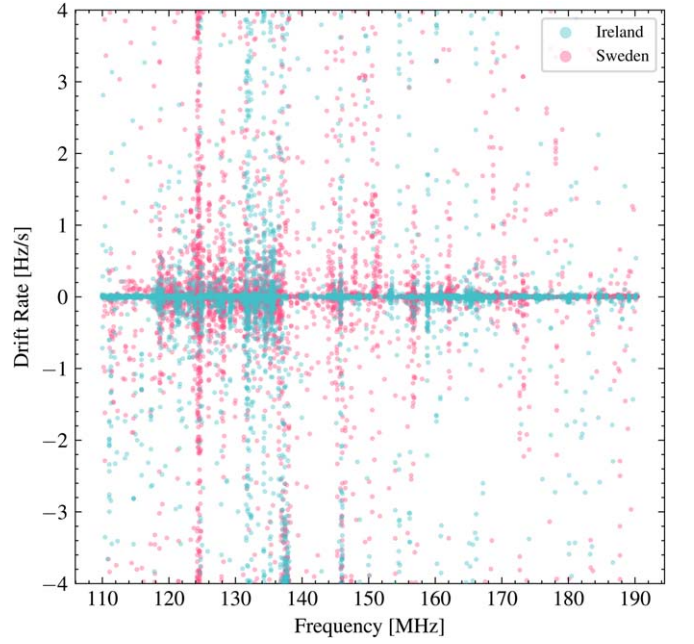


Figure 7. A scatter plot of the drift-rate values against detected frequency. The Irish station is shown in pink and the Swedish station is shown in blue.

4.3. Figure of Merit

To compare SETI surveys, Enriquez et al. (2017) introduced a figure of merit known as the Continuous Waveform Transmitter Rate (CWTFM),

$$\text{CWTFM} = \zeta_{\text{AO}} \frac{\text{EIRP}}{N_{\text{stars}} \nu_{\text{rel}}}, \quad (5)$$

where N_{stars} is the number of stars in each pointing for a given survey, and ν_{rel} is the fractional bandwidth of the survey, $\Delta\nu_{\text{tot}}/\nu_{\text{mid}}$, where ν_{mid} is the central frequency of the survey. ζ_{AO} is the normalization factor such that $\text{CWTFM} = 1$ and the EIRP is equal to the Arecibo radio telescope’s S-band planetary radar, if it were transmitted across a whole hemisphere, ($\sim 10^{13}$ W; Siemion et al. 2013). In Figure 11, we compare our results to those from some other SETI surveys. As this survey continues, the transmitter rate will decrease with the volume of stars observed (N_{stars}), as outlined by Equation (6):

$$\text{Transmitter Rate} = \log \left[\frac{1}{N_{\text{stars}} \cdot \nu_{\text{rel}}} \right]. \quad (6)$$

As dictated by Equation (4), to be sensitive to lower-powered ETI transmitters, the observation sensitivity needs to be greater. This can be done by employing further LOFAR stations for n -site simultaneous observations through coherent summation.

4.4. 110–190 MHz Technosignature Parameter Space

The number of intelligent civilizations is quantified using Equation (7), coined by Drake (1961):

$$N = R_* f_p N_e f_i f_c L. \quad (7)$$

In this expression, N is the number of communicative civilizations in the Milky Way galaxy, R_* is the rate of star

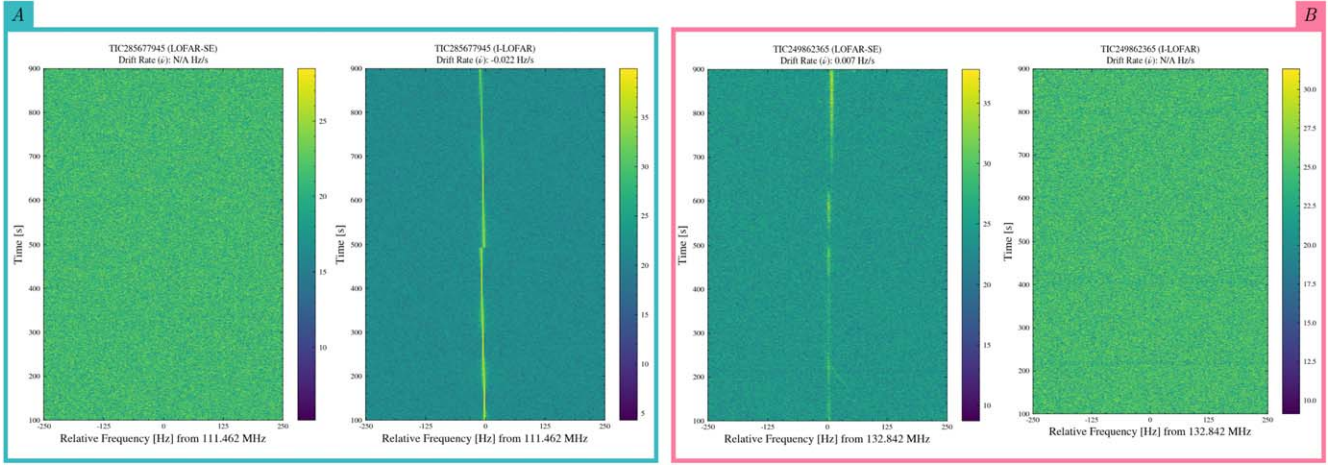


Figure 8. Dynamic spectra (waterfall plots) of detected narrowband signal centered on the detected frequency of detection, showing the two most common cases of coincidence rejection. Case A (left) shows a narrowband signal with a nonzero drift rate detected at I-LOFAR and not LOFAR-SE. Case B (Right) shows the opposite, where a nonzero drift-rate signal is not detected by I-LOFAR but is detected by LOFAR-SE. For a signal to be considered a detection of interest, both sites would have to exhibit nonzero drift-rate signal at the same frequency simultaneously.

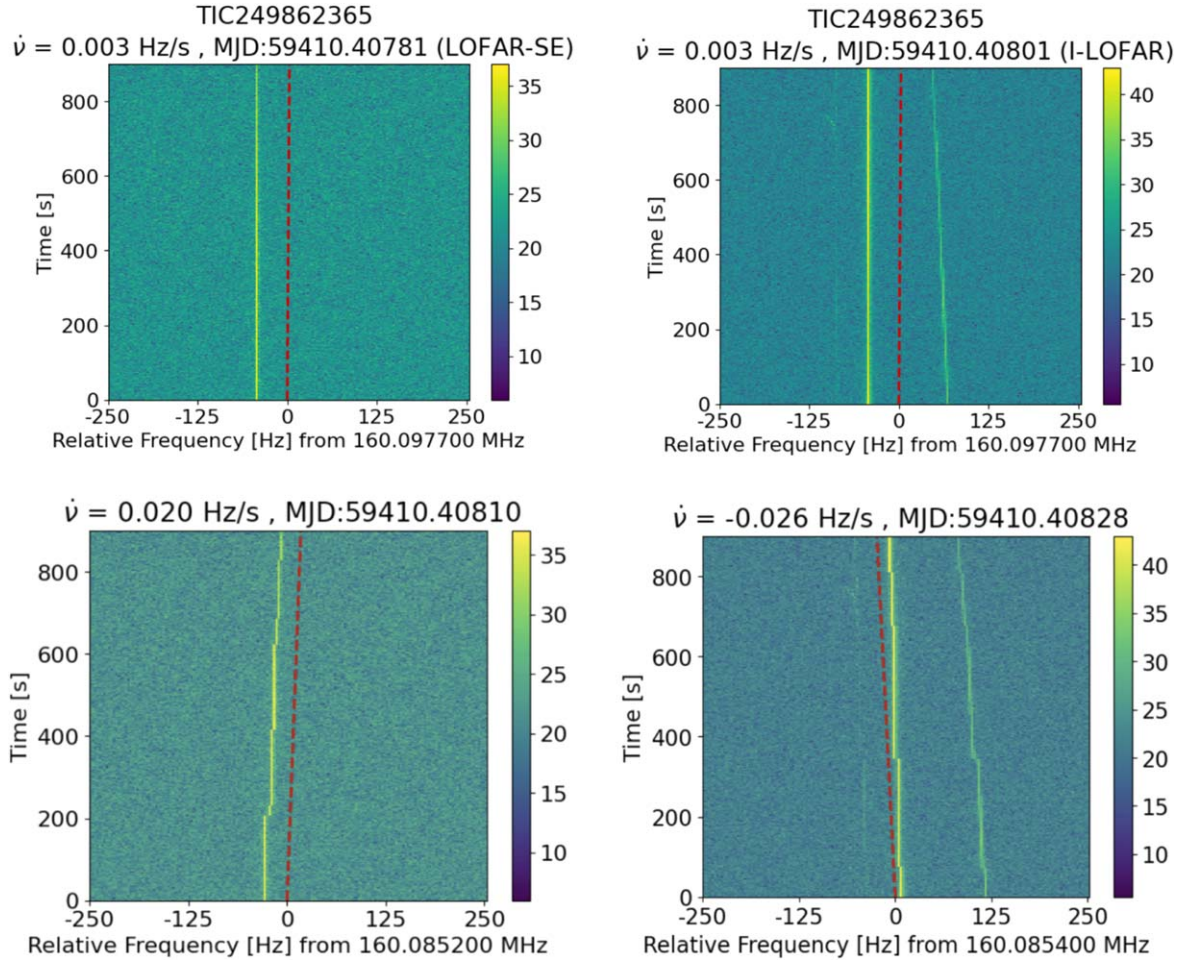


Figure 9. The top two plots represent narrowband signals detected at both stations in the topocentric frame of reference. The bottom two plots show the same detected narrowband signals detected at both stations but corrected to the barycentric frame of reference. This is illustrated by the newly added drift to signals present after correction.

formation per year in the galaxy, f_p is the fraction of stars that have planets around them, n_e is the average number of planets that can potentially support life per star that has planets, f_i is the

fraction of potentially life-supporting planets that actually develop life, f_l is the fraction of planets with life that go on to develop intelligent life, and f_c is the fraction of civilizations that

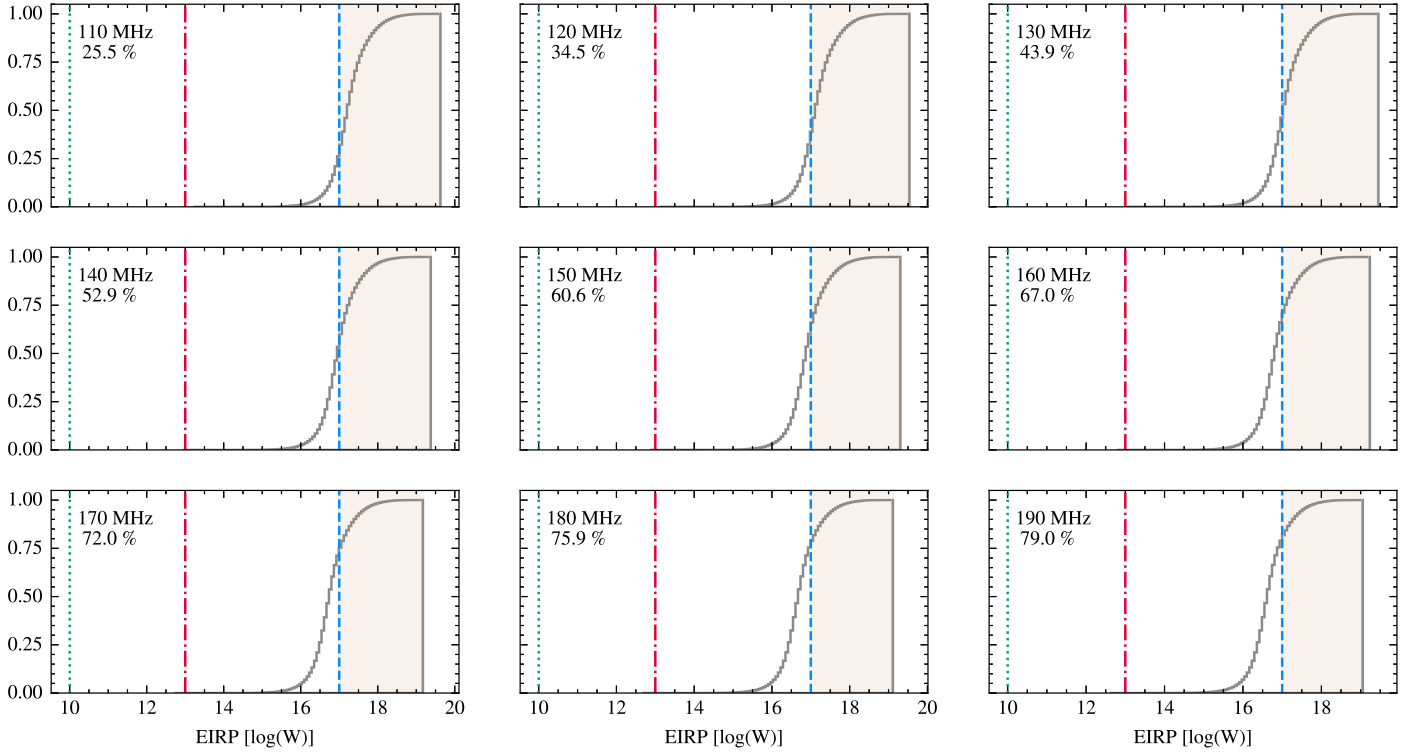


Figure 10. Cumulative histogram of EIRP limits of this survey across the HBA band. Reference luminosities for three civilization levels emitting 10^{17} , 10^{13} , or 10^{10} W are shown in blue, red, and green respectively. The percentage of targets where the station is sensitive to the transmission of 10^{17} W is shown, as a function of frequency across the band. At lower frequencies, sensitivity to 10^{17} emitters drops off as the T_{sys} rises. The T_{sys} varies from 1260 K down to 322 K as frequency is increased across the band. Detailed calculations are presented in Appendix B and Table B1.

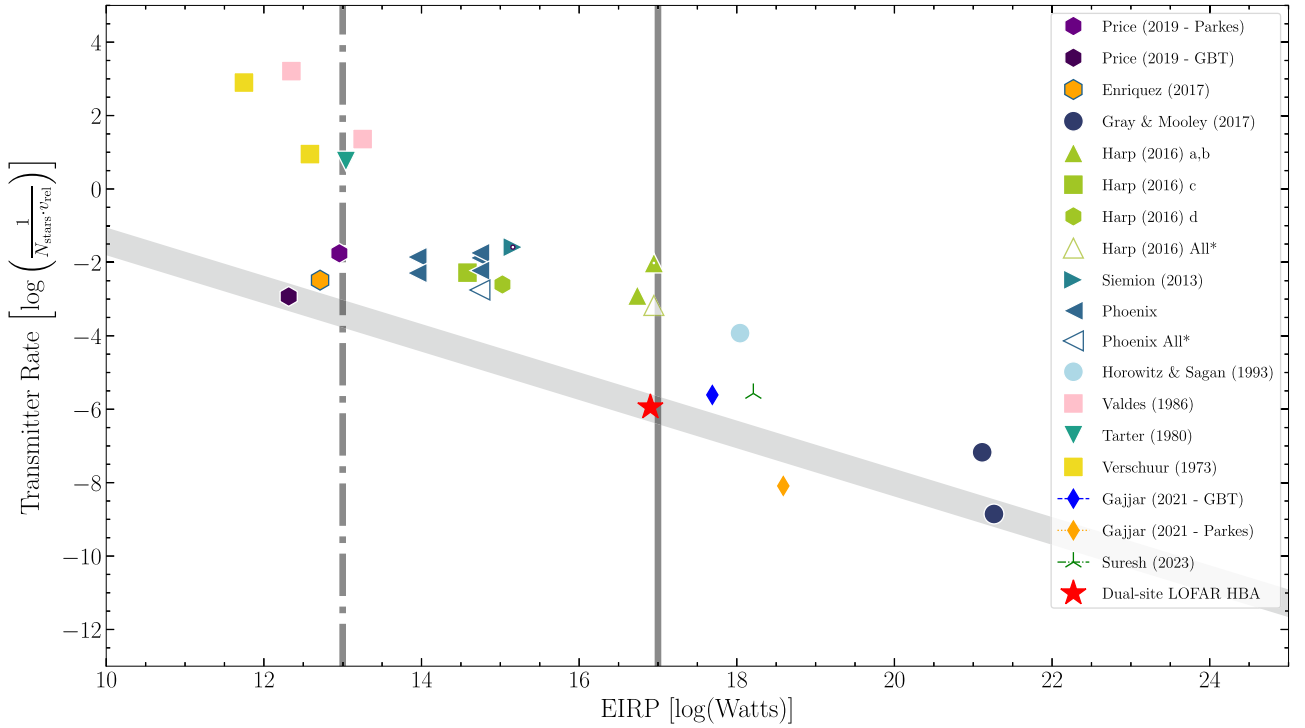


Figure 11. Comparison of our study (highlighted in red) to prior surveys. The plot presents the transmitter rate vs. EIRP, with the gray line indicating the transmitter rate as a function of EIRP. A solid vertical gray line illustrates the energy surplus of a Kardashev Type-I civilization. Additionally, a dotted-dashed gray line depicts the EIRP of the Arecibo planetary radar. The gray thick line shows the slope of the transmitter rate as a function of their EIRP power. Distance used for EIRP calculation is $\bar{d} + d_{\sigma} = 7009$ ly.

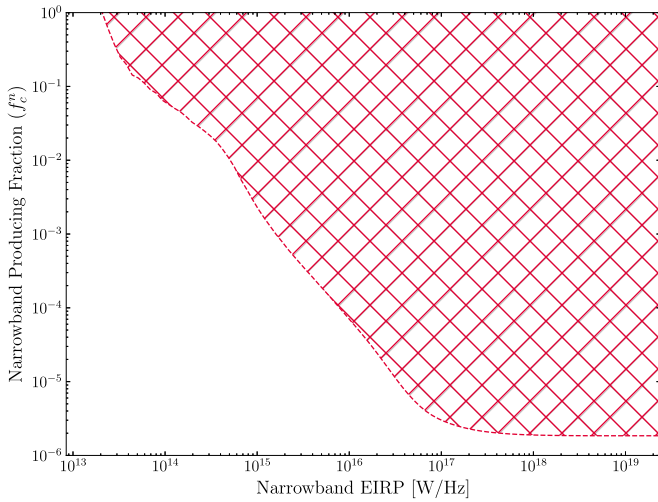


Figure 12. The fraction of stars that produce narrowband emission (f_c^n) against the transmitter power of the total target pool. The hashed region (red) shows the constraints this survey places on a value of f_c^n at 110–190 MHz.

develop a technology that releases detectable signs of their existence into space.

In Gajjar et al. (2022), a modified variation of the Drake equation (Equation (8); Shklovskii & Sagan 1966) is used to constrain the fraction of narrowband emitting civilizations (f_c^n):

$$N = R_{\text{IP}} f_c^n L. \quad (8)$$

Here, R_{IP} is defined as the emergence rate (yr^{-1}) of intelligent life in the Milky Way. Figure 12 shows the constraint that this survey places on f_c^n when using a Poisson one-sided upper limit at 95% confidence, which in this case is 2.995 as per Gehrels (1986). This provides the most stringent constraint of f_c^n in this frequency range.

4.5. Future Work Using LOFAR 2.0

LOFAR is soon to undergo a staged series of upgrades across all stations in the array. These upgrades at individual stations across Europe will involve the installation of a new Receiver Control Unit (RCU) as described in ASTRON (2023). These RCUs will enable the simultaneous use of both the LBA and HBA in the frequency range of 15–240 MHz. This enhancement will allow for a SETI survey across a broader low-frequency band.

Specifically, at 30 MHz, the FWHM will cover an area of 19.39 deg^2 , decreasing to 1.73 deg^2 at 190 MHz. This will enable follow-up LOFAR surveys to encompass a larger volume of stars and a broader frequency domain.

5. Conclusion

This paper presents a SETI search in a parameter space mostly unexplored by other SETI surveys (Price et al. 2018; Gajjar et al. 2021), by simultaneously observing TESS and Gaia targets of interest in the 110–190 MHz radio window. It also demonstrates dual-site coincidence rejection, showing that it provides a new method to discriminate candidate extra-terrestrial signals from terrestrial radio frequency interference. We propose this method as a promising means of follow-up for confirmation of any candidates interest arising in this type of study or others in this frequency range. Each target within our fields was then searched for narrowband signals at each station

using our most up-to-date search techniques (Enriquez et al. 2017). The benefit of barycentric correction for eliminating false positives is also demonstrated. Finally, the first stringent constraints on the fraction of transmitting civilizations at this frequency range have been shown, further constraining the parameter space the Drake equation presents.

As the LOFAR SETI observation campaign continues and more high-resolution frequency data are collected, a machine-learning search method comparable to that of Ma et al. (2023) can be trained and implemented to seek out signals of interest. Multiple LOFAR stations, or indeed subarrays of any other wide-footprint radio array, allow the option for a coincidence rejection method over the “ON” and “OFF” beam pointings used previously. For future low-frequency SETI surveys, the use of further international stations and a prolonged observation campaign will place even further constraints on an ETI residing in this parameter space. The addition of one or more LOFAR stations would allow for the use of localizing a signal of interest in the u - v plane, which would be useful for follow-up observations. This would be done post-facto through correlation of saved voltages for any candidates of interest.

Acknowledgments

Breakthrough Listen is managed by the Breakthrough Initiatives, sponsored by the Breakthrough Prize Foundation. D.J.McK. and A.B. are supported by Government of Ireland Studentships from the Irish Research Council (IRC). I-LOFAR has received funding from Science Foundation Ireland (SFI), the Department of Further and Higher Education, Research, Innovation and Science (DFHERIS) of the Government of Ireland. We acknowledge support from Onsala Space Observatory for the provisioning of its facilities and observational support. The Onsala Space Observatory national research infrastructure is funded through Swedish Research Council grant No. 2017-00648. This research has made use of the NASA Exoplanet Archive, which is operated by the California Institute of Technology, under contract with the National Aeronautics and Space Administration under the Exoplanet Exploration Program. This work also presents results from the European Space Agency (ESA) space mission Gaia. Gaia data are being processed by the Gaia Data Processing and Analysis Consortium (DPAC). Funding for the DPAC is provided by national institutions, in particular the institutions participating in the Gaia MultiLateral Agreement (MLA). This work has relied on NASA’s Astrophysics Data System (ADS) Bibliographic Services and the ArXiv. This work has made use of the VizieR catalog access tool, CDS, Strasbourg, France. The original description of the VizieR service was published in A&AS 143, 23. We also acknowledge the support and comments from Laura C. Cotter and the Berkeley SETI REU Program, classes of 2021 and 2022. We also thank the anonymous reviewers for their careful reading of our manuscript and their many insightful comments and suggestions.

Facility: LOFAR Stations IE613 and SE607.

Software: sigproc (Lorimer 2011), udpPacketManager (McKenna et al. 2023a), turboSETI (Enriquez et al. 2017), blimp (Price et al. 2019), astropy (Astropy Collaboration et al. 2022), astroquery (Ginsburg et al. 2019), pandas (pandas development team 2020).

Appendix A

Post-detection Barycentric Correction

We have developed a novel barycentric correction code specifically designed for high-spectral resolution `sigproc` filterbank products for technosignature searches (Gajjar 2023). The code uses the TEMPO routine to calculate relative velocity toward the observing targets at both locations, thus allowing for precise correction of the barycentric drift.

The Doppler shift caused by the relative motion between the transmitter and receiver will change over time as it is observed. Over a longer time frame, these shifts will exhibit a sinusoidal curve with a sidereal year period. Over a shorter time frame, the same pattern (superimposed on the yearly pattern) will be visible, but with a sidereal day period. Consequently, the relative velocity will change during the observation period, thereby altering the observed frequency of the received narrowband signal. This leads to a drift in the narrowband signal observed by the observer. Figure A1 displays examples of observed drifts at four different epochs for the same narrowband signal source observed from the same location. It is evident that, if the relative velocity is positive and increasing with time (leftmost plot in Figure A1), the signal, which is stationary in the barycentric frame, will drift toward lower frequencies as time progresses in the topocentric frame, as per Equation (3).

A.1. Algorithm Outline

Figure A2 shows an example of how data are arranged in a filterbank file. For our case, we will assume that, in a given filterbank file, frequency channels are in descending order with the first channel (f_1) having the highest frequency for each time sample. The goal of our tool is to shift every frequency channel from the observing frame to the actual emitted frequency frame after correcting for the barycentric relative velocity to remove any additional narrowband signal drift introduced by it. We aim to keep the first channel frequency of all the time samples the same in the barycentric frame also, and thus relative shifts

between spectras are needed to apply for each time sample corresponding to the inferred relative velocities. Our tool measures relative velocity at each time sample toward a given direction in the sky from a given telescope at the time of observations. Let us assume an observing scenario where $v_{\text{rel}} > 0$. Following Equation (3), we can state that the emitted frequency (or barycentric frequency) will be higher than the observed frequency. That means that observations stored in the first topocentric frequency channel correspond to higher barycentric frequency. Thus, this spectra needs to be shifted to higher frequency. If the relative velocity increases with time, the consecutive time sample's first channel barycentric frequency will be slightly higher than the previous sample's first channel emitted frequency. Our tool thus shifts the spectra of each time sample toward higher frequency such that the first channel's emitted frequency matches across all time samples. Due to these shifts, we either replace empty channels at the edge of the spectra with zeros in cases of squeeze or drop extra channels in cases of expansion.

As given in Equation (3), the Doppler shifts are frequency-dependent, impacting higher frequencies more than lower frequencies. In other words, for spectra where frequencies are ordered from higher to lower frequency, the first channel will be shifted more compared to the last frequency channel. To compensate for this, we either expand or squeeze spectra as shown in Figure A3. Figure A4 outlines the logical flow of the code for a case of an input filterbank file with a descending order of frequency. By comparing Figure A1 and the code outline in Figure A4, we can consider one of the cases where the relative velocity is negative and increasing in absolute value with time. In this case, we need to shift consecutive spectra to lower and lower frequencies in order to match up their first frequency channel. Furthermore, for any negative relative velocity (either increasing or decreasing with time), we need to squeeze the individual spectra as shown in Figure A3. Similarly, the same can be considered for the case of positive relative velocity. The code for this algorithm is publicly available here.²²

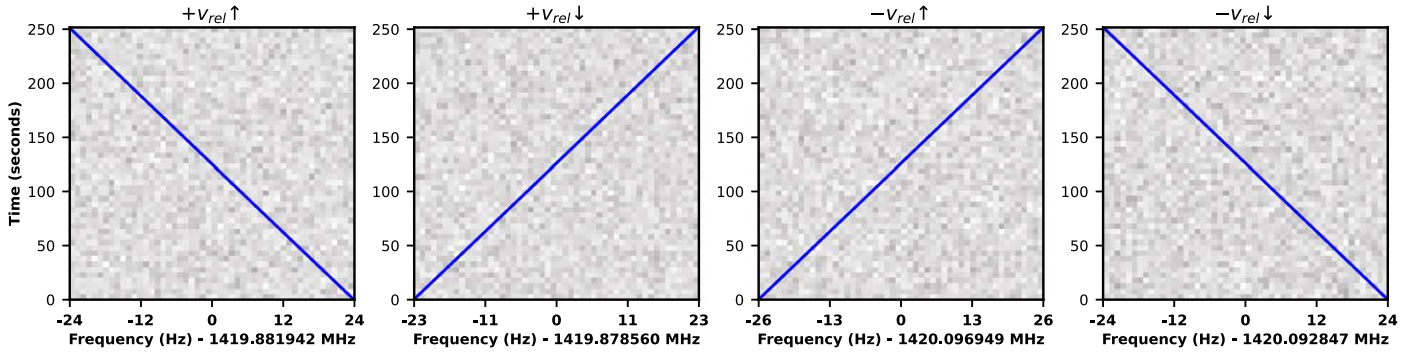


Figure A1. Doppler drift of a narrowband signal in the topocentric observing frame at four different observing epochs. Simulated waterfalls with narrowband signals observed from the Irish LOFAR station toward the direction of TIC 27677846 are shown for different times of the year in blue. The expected sign and direction of change of the relative velocity are labeled at the top of each plot. It is assumed that a hypothetical narrowband ETI signal is transmitted at a constant frequency of 1420 MHz (with zero drift rate). As shown, the same signal is observed at different frequencies and drift rates depending on the sign and direction of change of the relative velocity at different epochs of observations. For instance, in the first panel, the relative velocity is positive and increases with observing time. Therefore, the observing frequency has been shifted to a lower frequency (as described by Equation (3)), and it continues to shift to even lower frequencies with time.

²² <https://github.com/gajjar/BaryCentricCorrection>

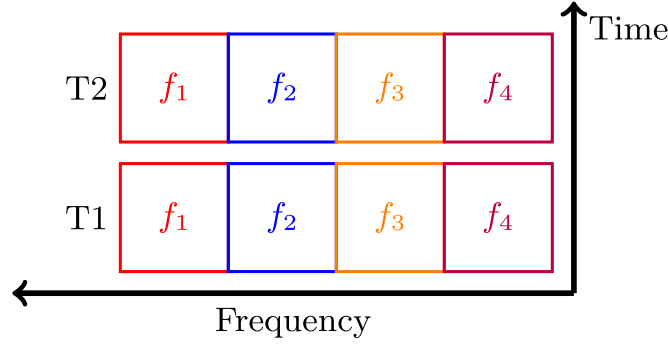


Figure A2. A typical filterbank file stores data in a time and frequency matrix format. Each row represents a sample, while each column represents a frequency channel for a given sample. Time is increasing from bottom to top, while the frequency is increasing from right to left.

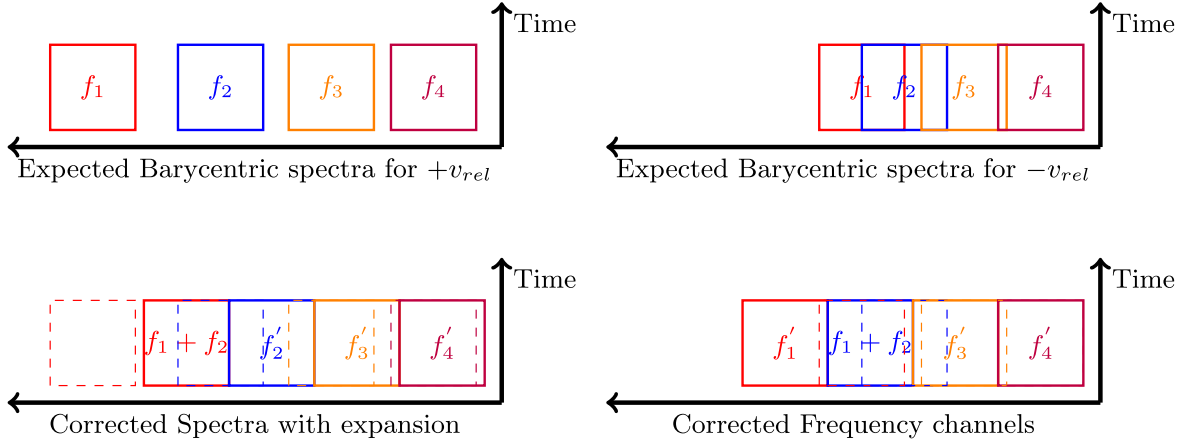


Figure A3. These plots depict the expected spectra at their respective barycentric frequencies and the spectra after the correction for barycentric relative velocity. Each plot represents a single spectrum, where the frequency increases from right to left. (a) In the case of $+v_{rel}$, the first channel of the topocentric spectra is shifted to a higher barycentric frequency compared to the last topocentric spectra channel, which causes an expansion of the spectra. If two consecutive channels move farther away from each other (shown as f_1 and f_2) by more than half the channel width, an additional channel is added in between, which is the summation of these two channels. Extra channels at the edge of the spectra are dropped. (b) In the case of $-v_{rel}$, the first channel of the topocentric frequency is shifted to a lower barycentric frequency relative to the last topocentric spectra channel, which causes a squeeze in the spectra. If two consecutive frequency channels shift closer to each other by more than half a channel width, these channels are added together and an extra channel is added at the end containing zeros. The bottom spectra in each plot illustrate these expansion and squeeze effects after correction are applied from the code.

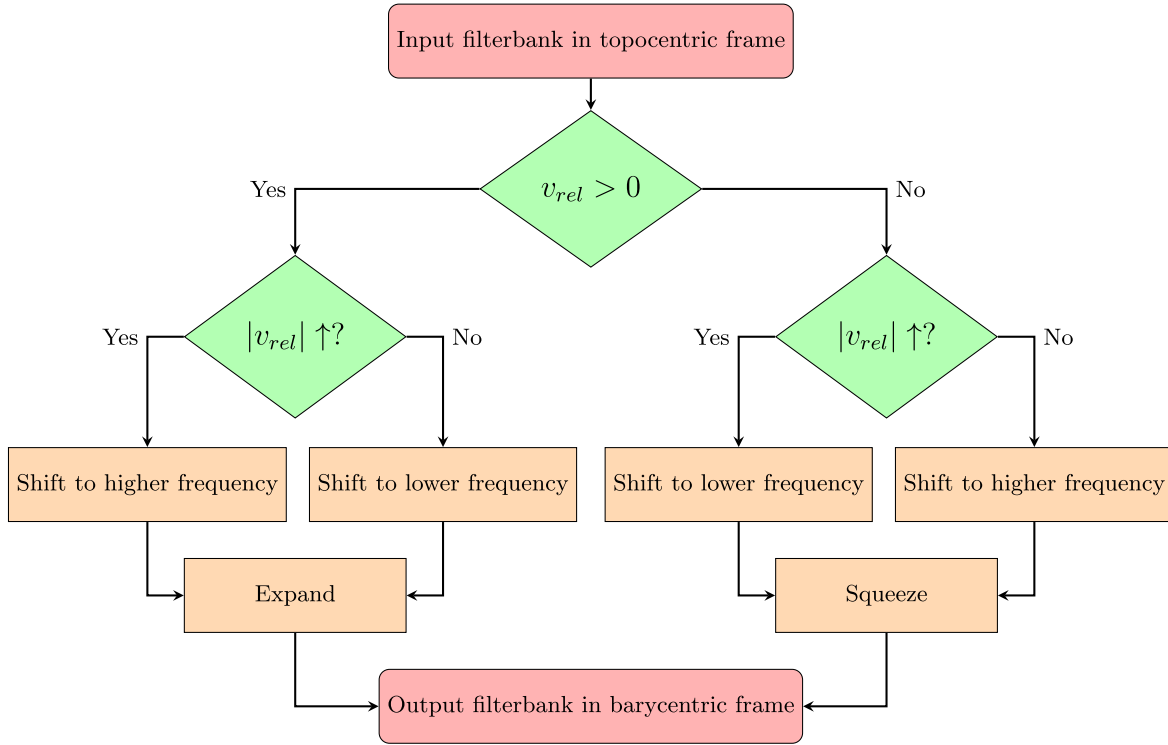


Figure A4. An outline of the post-detection barycentric correction algorithm for an input filterbank file in `sigproc` format. For this case, the input filterbank file has a descending order in frequency, and v_{rel} represents the relative velocity between the transmitter and observer. The algorithm considers two cases depending on whether the relative velocity is positive or negative, which indicates whether the source is moving away from or toward the observer, respectively. Each of these cases is further divided into two, where the absolute value of the relative velocity can either increase or decrease, requiring the spectra to be shifted to either the higher- or lower-frequency end. For all cases with $+v_{\text{rel}}$, each spectra is expanded, and for $-v_{\text{rel}}$, each spectra is squeezed, as shown in Figure A3. The code then writes each of these spectra into another `sigproc` filterbank file, which will have each channel frequency closely corrected to the barycentric frame of reference.

Appendix B

Sensitivity of the Survey across the HBA

As previously stated, the high-band antenna spans from 110 to 190 MHz. The system temperature across the band significantly, which reduces the sensitivity of LOFAR at the lower end of the bandpass (see. Figure 10). Calculation of T_{sys} and consequently SEFD follows a modified method, as outlined in Section 3.3 of McKenna et al. (2023b). The method differs in the calculation of T_{sky} , as this is pointing dependent. This study

uses the LWA1 Low Frequency Sky Survey (Dowell et al. 2017) for sensitivity analysis. We calculate system equivalent flux density (SEFD; Jy) as follows:

$$\text{SEFD} = \frac{2T_{\text{sys}}k_b}{A_e}, \quad (\text{B1})$$

where k_b is the Boltzmann constant and A_e is the effective collecting area of a single station HBA. EIRP is then consequently calculated using Equation (4).

Table B1
Statistics on Sensitivity across the HBA Band

Frequency (MHz)	110	120	130	140	150	160	170	180	190
\bar{T}_{sys} (K)	1305.073	1051.633	862.204	717.304	604.260	514.594	442.408	383.552	335.019
SEFD (Jy)	2148.125	1730.967	1419.171	1180.668	994.601	847.011	728.195	631.320	551.435
EIRP (W)	17.273	17.179	17.092	17.011	16.937	16.866	16.801	16.738	16.679
EIRP _{median} (W)	17.235	17.141	17.054	16.974	16.899	16.829	16.763	16.701	16.642
EIRP _{max} (W)	19.628	19.537	19.454	19.377	19.304	19.237	19.173	19.112	19.055
EIRP _{min} (W)	12.627	12.627	12.627	12.627	12.627	12.627	12.627	12.627	12.627
K1 detectable (%)	25.497	34.493	43.910	52.859	60.644	66.968	71.969	75.887	79.032
Earth detectable (%)	14.659	20.613	27.730	35.694	43.908	51.781	58.826	64.739	69.612

Note. The K1 and Earth detectable values represent the percentages of the target sample that are detectable.

ORCID iDs

Owen A. Johnson  <https://orcid.org/0000-0002-5927-0481>
 Vishal Gajjar  <https://orcid.org/0000-0002-8604-106X>
 Evan F. Keane  <https://orcid.org/0000-0002-4553-655X>
 David J. McKenna  <https://orcid.org/0000-0001-7185-1310>
 Charles Giese  <https://orcid.org/0000-0003-1517-8891>
 Ben McKeon  <https://orcid.org/0000-0001-7060-4852>
 Tobia D. Carozzi  <https://orcid.org/0000-0002-4963-179X>
 Cloe Alcaria  <https://orcid.org/0000-0001-6299-5726>
 Aoife Brennan  <https://orcid.org/0000-0002-7050-0161>
 Bryan Brzycki  <https://orcid.org/0000-0002-7461-107X>
 Steve Croft  <https://orcid.org/0000-0003-4823-129X>
 Peter T. Gallagher  <https://orcid.org/0000-0001-9745-0400>
 Ruth Kelly  <https://orcid.org/0000-0002-5004-3573>
 Matt Lebofsky  <https://orcid.org/0000-0002-7042-7566>
 Dave H. E. MacMahon  <https://orcid.org/0000-0001-6950-5072>
 Joseph McCauley  <https://orcid.org/0000-0003-4399-2233>
 Imke de Pater  <https://orcid.org/0000-0002-4278-3168>
 Shauna Rose Raeside  <https://orcid.org/0000-0002-0598-2061>
 Andrew P. V. Siemion  <https://orcid.org/0000-0003-2828-7720>

References

- Albareti, F. D., Allende Prieto, C., Almeida, A., et al. 2017, *ApJS*, **233**, 25
 ASTRON 2023, LOFAR2.0 White Paper - v2023.1, https://www.lofar.eu/wp-content/uploads/2023/04/LOFAR2_0_White_Paper_v2023.1.pdf
 Astropy Collaboration, Price-Whelan, A. M., & Lim, P. L. 2022, *ApJ*, **935**, 167
 Bailer-Jones, C. A. L., Rybizki, J., Fousneau, M., Mantelet, G., & Andrae, R. 2018, *AJ*, **156**, 58
 Borucki, W., Koch, D., Basri, G., et al. 2008, in IAU Symp. 249, Exoplanets: Detection, Formation and Dynamics, ed. Y. S. Sun, S. Ferraz-Mello, & J. L. Zhou (Cambridge: Cambridge Univ. Press), 17
 Burke, B. F., Graham-Smith, F., & Wilkinson, P. N. 2019, An Introduction to Radio Astronomy (4th edn.; Cambridge: Cambridge Univ. Press),
 Di Vruono, F., Winkel, B., Bassa, C. G., et al. 2023, *A&A*, **676**, A75
 Dowell, J., Taylor, G. B., Schinzel, F. K., Kassim, N. E., & Stovall, K. 2017, *MNRAS*, **469**, 4537
 Drake, F. D. 1961, *PhT*, **14**, 40
 Enriquez, J. E., Siemion, A., Foster, G., et al. 2017, *ApJ*, **849**, 104
 Gajjar, V. 2023, Post-detection barycentric correction, Zenodo, doi:10.5281/ZENODO.8290103
 Gajjar, V., LeDuc, D., Chen, J., et al. 2022, *ApJ*, **932**, 81
 Gajjar, V., Perez, K. I., Siemion, A. P. V., et al. 2021, *AJ*, **162**, 33
 Gajjar, V., Siemion, A., Croft, S., et al. 2019, *BAAS*, **51**, 223
 Gehrels, N. 1986, *ApJ*, **303**, 336
 Ginsburg, A., Sipőcz, B. M., Brasseur, C. E., et al. 2019, *AJ*, **157**, 98
 Gaia Collaboration, Babusiaux, C., van Leeuwen, F., et al. 2018, *A&A*, **616**, A10
 Gaia Collaboration, Vallenari, A., Brown, A. G. A., et al. 2023, *A&A*, **674**, A1
 Johnson, O. 2023, D-SOP: Dual Site Observation Planner, Zenodo, 10.5281/ZENODO.8296753
 Kasting, J. F., Whitmire, D. P., & Reynolds, R. T. 1993, *Icar*, **101**, 108
 Lebofsky, M., Croft, S., Siemion, A. P. V., et al. 2019, *PASP*, **131**, 124505
 Li, J. K., Zhao, H. C., Tao, Z. Z., Zhang, T. J., & Xiao-Hui, S. 2022, *ApJ*, **938**, 1
 Loeb, A., & Zaldarriaga, M. 2007, *JCAP*, **2007**, 020
 Lorimer, D. R. 2011, SIGPROC: Pulsar Signal Processing Programs, Astrophysics Source Code Library, ascl:1107.016
 Ma, P., Ng, C., Rizk, L., et al. 2023, *NatAs*, **7**, 492
 McKenna, D. J., Keane, E. F., Gallagher, P. T., & McAuley, J. 2023a, arXiv:2309.03228
 McKenna, D. J., Keane, E. F., Gallagher, P. T., & McCauley, J. 2023b, *MNRAS*, in press
 NASA Exoplanet Science Institute 2022, Planetary Systems Table, IPAC, <https://exoplanetarchive.ipac.caltech.edu/>
 Ng, C., Rizk, L., Mannion, C., & Keane, E. F. 2022, *AJ*, **164**, 205
 pandas development team, T 2020, pandas-dev/pandas: Pandas, v1.5.2, Zenodo, 10.5281/zenodo.3509134
 Price, D., Enriquez, J., Chen, Y., & Siebert, M. 2019, *JOSS*, **4**, 1554
 Price, D. C., Enriquez, J. E., Brzycki, B., et al. 2020, *AJ*, **159**, 86
 Price, D. C., MacMahon, D. H. E., Lebofsky, M., et al. 2018, *PASA*, **35**, e041
 Ricker, G. R., Winn, J. N., Vanderspek, R., et al. 2015, *JATIS*, **1**, 014003
 Sheikh, S. Z., Wright, J. T., Siemion, A., & Enriquez, J. E. 2019, *ApJ*, **884**, 14
 Shklovskii, I. S., & Sagan, C. 1966, Intelligent Life in the Universe (1st edn.; New York: Dell Publishing)
 Siemion, A. P. V., Demorest, P., Korpela, E., et al. 2013, *ApJ*, **767**, 94
 Tarter, J., Cuzzi, J., Black, D., & Clark, T. 1980, *Icar*, **42**, 136
 Tarter, J. C. 1996, *Proc. SPIE*, **24**
 Tingay, S. J., Goeke, R., Bowman, J. D., et al. 2013, *PASA*, **30**, e007
 Tingay, S. J., Tremblay, C., Walsh, A., & Urquhart, R. 2016, *ApJL*, **827**, L22
 Tingay, S. J., Tremblay, C. D., & Croft, S. 2018a, *ApJ*, **856**, 31
 Tingay, S. J., Kaplan, D. L., Lenc, E., et al. 2018b, *ApJ*, **857**, 11
 van Haarlem, M. P., Wise, M. W., Gunst, A. W., et al. 2013, *A&A*, **556**, A2
 Włodarczyk-Sroka, B. S., Garrett, M. A., & Siemion, A. P. V. 2020, *MNRAS*, **498**, 5720
 Wordsworth, R., & Pierrehumbert, R. 2014, *ApJL*, **785**, L20
 Wright, J. T. 2018, Exoplanets and SETI (Berlin: Springer), 186